Hindawi
Shock and Vibration
Volume 2018, Article ID 6454932, 17 pages
https://doi.org/10.1155/2018/6454932

Research Article

Characteristics, Optimal Design, and Performance Analyses of MRF Damper

Xin De-kui, Nie Song-lin, Ji Hui, and Yin Fang-long

Beijing Key Laboratory of Advanced Manufacturing Technology, Beijing University of Technology, Beijing 100124, China

Correspondence should be addressed to Ji Hui; jihui@bjut.edu.cn

Received 3 March 2018; Revised 30 April 2018; Accepted 16 May 2018; Published 27 June 2018

Academic Editor: Gabriele Cazzulani

Magnetorheological fluid (MRF) damper is one of the most promising semiactive devices for vibration control. In this paper, a shear-valve mode MRF damper for pipeline vibration control is proposed. The dynamic model and the state equation of the pipeline are established and the linear quadratic regulator (LQR) is used to generate the optimal damping force of MRF damper. The design concept considering the structure and the electromagnetic properties simultaneously is discussed in detail. A mathematical model of the relation between shear stress and control current based on interpolation method is established. Finite element analysis (FEA) software COMSOL is selected to simulate the magnetic field and electromagnetism-thermal field of the MRF damper. A computational method based on the simulation model is established to calculate the shear stress. In order to reduce the magnetic leakage, a method of adding magnetism-insulators at both ends of the piston head is presented. The influence of control current, displacement, and velocity on mechanical performance of the proposed MRF damper is experimentally investigated. The test results show that the performance of the MRF damper is basically identical with the theoretical prospective and the simulation conclusions, which proves the correctness and feasibility of this design concept.

1. Introduction

Magnetorheological fluid (MRF) is a new kind of intelligent fluid that consists of microscale magnetic particles suspended in a carrier liquid such as oil, water, or glycol [1]. The rheological characteristics of MRF could be rapidly and reversibly altered when an external magnetic field is applied, making MRF an excellent working fluid for mechanical vibration damping and shock isolation devices [2]. The damper using MRF as working liquid has the advantages of low energy consumption, fast response, simple structure, adjustable damping force, and broad temperature range [3, 4]. MRF dampers based semiactive control systems could approach the effectiveness of an active control system without requiring heavy power supply. Moreover, even if the power failure occurs, it can still work as a passive damping device to prevent the system from damage, which makes the system have high-intelligence and high-reliability [5]. With these advantages, MRF dampers have been widely investigated for such application as vibration and shock control, high-rise building antivibration, stay cable vibration control, vehicle suspension system, offshore platform structure vibration damping, seat suspensions, weapon recoil systems, precision machining, and crash worthiness systems [6, 7]. Similarly, by installing MRF dampers in pipeline system and applying vibration control strategy to adjust the damping force of MRF dampers according to the vibration characteristics of the pipeline, the pipeline vibration could be controlled, the fatigue fracture of the pipeline and loosening of the pipe joints could be suppressed, the fluid leakage in the pipeline could be prevented, and the pipeline system could be run more safely and stably. However, the MRF damper will convert mechanical vibration energy into heat energy during the working process. In addition, the electronic control system is an essential part of the MRF damping system. However the control current, control voltage, and power consumption MRF dampers are relatively low and will not produce high temperature or arc during operation [8]. But, for industrial applications such as oil, gas, and chemical industry, the MRF damper and its control circuit must be designed for explosion protection according to the requirements of the explosion-proof class [9].

In the presence of the magnetic field within a few milliseconds MRF could exchange to semisolid state of chain-like fibrous structure from free-flowing state and typically exhibit similar rheological behavior to Bingham fluid; besides, the transition is reversible [10]. Therefore, the attempts to determine the principal design parameters of the MRF dampers based on the Bingham model have been made by numerous researchers [11]. Although the rheological behavior of MRF actually exhibits some departures from the Bingham model and it is not sufficient to describe the MRF damper nonlinear behavior under dynamic loading, specifically the nonlinear force-velocity behavior, it has been proved that this simple model is very useful for the design and modeling of MRF based devices [12]. However, due the nonlinearity of the magnetic hysteresis characteristic of the damper structure materials and the MRF, the distribution of magnetic field in the MRF damper is not uniform, and the shear yield strength of MRF increases nonlinearly with an increase of the applied magnetic field; it is very difficult to solve the magnetic circuit of the MRF damper analytically [13]. In order to describe the nonlinear hysteresis dynamic behavior of MRF dampers, several dynamic models have been proposed, such as Bouc-Wen model and LuGre model [14]. However, these dynamic models are experiment based models. Thus, parameters of the models are derived based on experimental results of a real damper [15]. Therefore, in order to improve the performance of the MRF damper and to effectively control its damping force, it is necessary that the magnetization properties of the magnetic circuit are considered in the design phase [16, 17]. The finite element numerical simulation has become one of the effective ways to solve complex geophysical problems for scientific research and engineering computing [18, 19]. During finite element simulation (FES) the interconnections of fields are taken into account in the form of feedback in accordance with the results of the certain fields calculation, in which structural parameters, electromagnetic coil parameters, and material properties of the MRF damper could be analyzed [20, 21].

In this paper, a double-ended and shear-valve mode MRF damper for pipeline vibration suppression is proposed. Firstly, the working principles of the MRF damper are introduced. The characteristic parameters of the MRF damper are emphatically discussed. The geometric parameters of the MRF damper are analytically determined considering the electromagnetic properties of the magnetic circuit. The mathematical model of the MRF damper is established using a Bingham plastic nonlinear fluid model and the function of the MRF damper is theoretically evaluated. Then, the finite element analysis is implemented with COMSOL 5.3, the magnetic field and the Joule heat generated by electromagnetic circuit of the MRF damper are analyzed, and the performance of the MRF damper is also studied. Finally, in order to validate the theoretical results predicted by the mathematical model and the simulation model, the prototype MRF damper is designed, fabricated, and tested.

2. Design and Analysis of the MRF Damper

2.1. Principle of Shear-Valve Mode MRF Damper. The pipeline damping suppression system based on MRF dampers is shown in **Figure 1**. Because the vibration direction of the pipeline is random, it is necessary for the MRF damper to have a high lateral load bearing capacity. For this reason, a double-ended and shear-valve mode MRF damper is proposed in this paper. The structure of the MRF damper is shown in **Figures 2** and **3**.

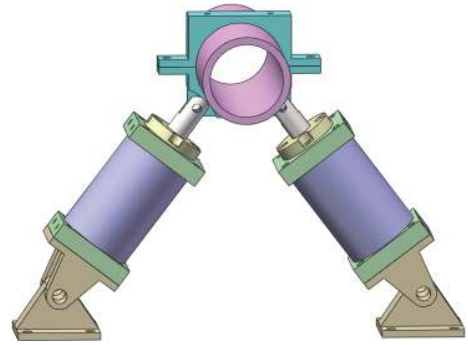

Figure 1: Pipeline damping suppression system.

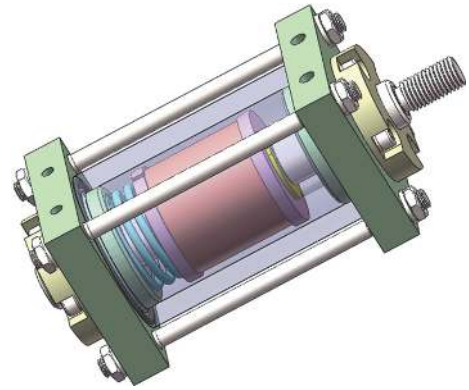

Figure 2: 3D model of the MRF damper.

As shown in **Figure 3**, the MRF damper is mainly composed of piston, electromagnetic coil, cylinder, and MRF. The internal magnetic field of the damper is excited by an electromagnetic coil wound around the middle of the piston yoke [22]. The winding part of the electromagnetic coil is the magnetic core. The magnetic flux generated by the exciting coil flows from the magnetic core to the damping gap (i.e., the annular gap between the piston and the cylinder) through the yoke flange. Then the magnetic flux flows into the cylinder wall through the damper gap and passes through the other side damping gap. Finally the magnetic flux flows back to the magnetic core, forming a closed magnetic circuit. This magnetic field changes the viscosity of MRF [23, 24] and, as a result, changes the force to push the piston through the MRF. As the current increases, the yield stress of the MRF increases, which causes more force to move the piston. Therefore, the damping force of the MRF damper could be controlled by adjusting the current applied to the exciting coil.

The total damping force F could be decomposed into a controllable force F_τ due to the controllable yield stress τ_y, an uncontrollable force F_η, and a friction F_f [25, 26]. According

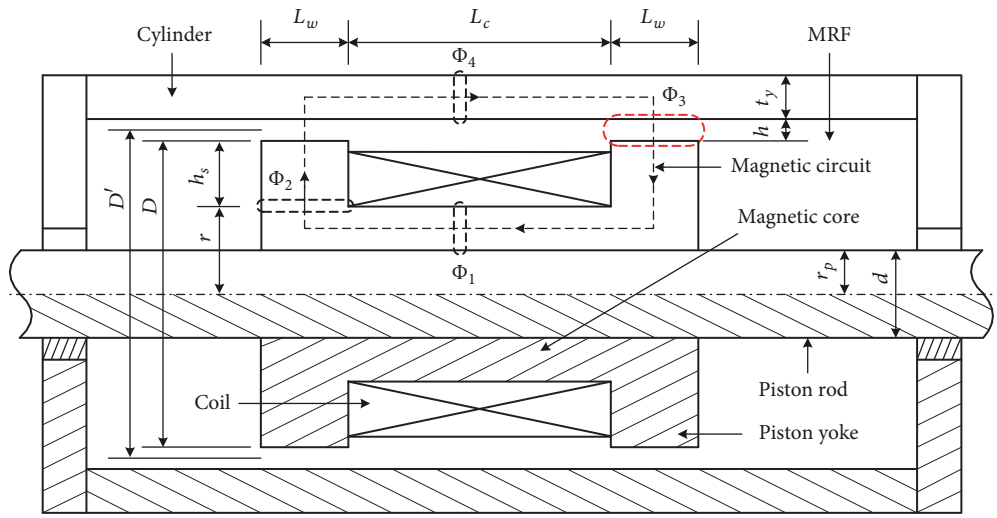

Figure 3: Schematic of shear-valve mode MRF damper.

to the parallel-plate Bingham model [27, 28], the damping force of the MRF damper can be expressed as

$$\begin{aligned} F &= F_\eta + F_\tau + F_f \\ &= \frac{12\eta L A_P^2}{\pi D' h^3} u + \left(\frac{3L\tau_y A_P}{h} + F_f \right) \operatorname{sgn}[u] \end{aligned} \tag{1}$$

where F_η is the viscous stress, F_τ is the shear stress, η is the dynamic viscosity of MRF, L is the effective length of piston, A_P is the effective area of piston, h is the width of damping gap, D' is the mean diameter of damping gap [29], and u is the relative velocity of piston and cylinder.

Damping force and dynamic range are two important indicators of MRF dampers; not only high damping force but also high dynamic range is necessary for the damping force control in the field of vibration control. The dynamic range of MRF damper could be written as [30]

$$\beta = \frac{F_\tau + F_\eta + F_f}{F_\eta + F_f} = 1 + \frac{F_\tau}{F_\eta + F_f} \tag{2}$$

where F_f is the friction force.

Equations (1) and (2) show that the damping force and the dynamic range of the shear-valve mode MRF damper mainly depend on the structural parameters and the performance of the MRF. In order to achieve high damping force and high dynamic range, the mechanical structure of the damper should be reasonable, and the MRF with high shear yield strength and low dynamic viscosity should be selected [31].

2.2. Magnetic Circuit Optimal Design of MRF Damper. The target in the design of the magnetic circuit is to achieve the optimum magnetic flux density at the effective areas. In order to improve the performance and reduce the volume of the MRF damper, the structure and electromagnetic design should be considered simultaneously. It is observed from **Figure 3** that the magnetic circuit of the shear-valve mode MRF dampers mainly consists of magnetic core, piston yoke, cylinder wall, and the MRF in the damping gap [32]. In order to effectively supply the magnetic field to the MRF, any part of the magnetic circuit should not reach magnetic saturation before the MRF in the damping gap. Based on the magnetic flux conservation rule in closed magnetic circuit [33] and ignoring the magnetic flux leakage, then

$$\Phi_1 = \Phi_2 = \Phi_3 = \Phi_4 \tag{3}$$

where Φ_1, Φ_2, Φ_3, and Φ_4 are the magnetic flux values in the respective locations, as shown in **Figure 3**. Corresponding expressions of magnetic flux in different locations are obtained based on the formulas of static magnetism.

$$\Phi_1 = \pi \left(r^2 - r_p^2 \right) B_p \tag{4}$$

$$\Phi_2 = 2\pi r L_w B_p \tag{5}$$

$$\Phi_3 = 2\pi \left(r + h_s \right) L_w B_m \tag{6}$$

$$\Phi_4 = \pi \left[\left(r + h_s + h + t_y \right)^2 - \left(r + h_s + h \right)^2 \right] B_y \tag{7}$$

where r is the radius of the magnetic core, L_w is the width of the yoke flange, h_s is the depth of the slot, t_y is the thickness of the cylinder wall, and B_m, B_p, and B_y are the saturation magnetic induction intensities of the MRF, the piston yoke, and the cylinder wall.

From (3) to (7),

$$L_w = \frac{r^2 - r_p^2}{2r} \tag{8}$$

$$h_s = \frac{\left(B_p - B_m \right) r}{B_m} \tag{9}$$

$$t_y = \sqrt{2\left(r + h_s \right) L_w \frac{B_m}{B_y} + \left(r + h + h_s \right)^2} - r - h - h_s \tag{10}$$

Table 1: Material properties of the MRF damper.

Component	Piston yoke, Cylinder	Piston rod	MRF	End cover	Magnetism insulator
Material	DT4C	Steel 45	MRF2035	Steel 304	Copper
Density (kg/m^3)	7870	7850	3640	7930	8700
Thermal conductivity (W/(m·K))	61	44.5	22.5	16.3	400
Heat capacity (J/(kg·K))	460	475	2000	500	385

From (4), (8), (9), and (10), it is observed that the volume of MRF dampers is largely dependent on the saturation magnetic induction intensity of the materials, especially the saturation magnetic induction intensity of the piston yoke and the cylinder wall.

The magnetic field generation is a key for all MRF devices. Consider the magnetic circuit of the MRF damper structure shown in **Figure 3**, neglecting magnetic flux leakage. The magnetic circuit of the shear-valve mode MRF damper could be analyzed using the magnetic Kirchhoff's law [34].

$$\begin{aligned} NI &= \Phi\left(R_P + R_m + R_y\right) \\ &= \Phi\left(\frac{L_w + L_c + h_s}{\mu_p S_p} + \frac{2h}{\mu_m S_m} + \frac{L_w + L_c}{\mu_y S_y}\right) \end{aligned} \tag{11}$$

where N is the number of coil turns, I is the current, Φ is the total magnetic flux, L_c is the coil length, and μ_m, μ_P, and μ_c are the permeabilities of the MRF, the piston yoke, and the cylinder wall, respectively. S_p, S_m, and S_y are the cross-sectional areas of the piston yoke, the damping gap, and the cylinder wall. R_p, R_m, and R_y are the magnetoresistance of the piston yoke, the MRF in the damping gap, and the cylinder wall.

According to the Gauss law of magnetic field, the magnetic flux at the damping gap could be expressed as

$$\Phi = B_m S_m \tag{12}$$

Since the permeabilities of the piston yoke and cylinder wall are far greater than that of the MRF, the magnetoresistance of the piston yoke and cylinder wall in (11) could be neglected. From (11) and (12), the number of the coil turns could be expressed as

$$N = \frac{2B_m h}{\mu_m I} \tag{13}$$

2.3. Configuration of MRF Damper. For a general n degree of freedom pipeline system, the controlled structural motion equation under environmental disturbance $F(t)$ and control force $U(t)$ could be expressed as

$$M\ddot{X}(t) + C\dot{X}(t) + KX(t) = D_s F(t) + B_s U(t) \tag{14}$$

where $X(t)$, $\dot{X}(t)$, and $\ddot{X}(t)$ are displacement, velocity, and acceleration vector of the pipeline system, respectively. M, C, and K are mass, damping, and stiffness matrices of the pipeline system, respectively. B_s is the location matrix of MRF dampers, and D_s is the disturbance matrix.

In the state space representation, (14) can be expressed as

$$\begin{aligned} \dot{Z}(t) &= AZ(t) + BU(t) + DF(t) \\ Z(t_0) &= Z_0 \end{aligned} \tag{15}$$

in which

$$\begin{aligned} Z(t) &= \begin{bmatrix} X(t) \\ \dot{X}(t) \end{bmatrix}, \\ A &= \begin{bmatrix} 0_n & I_n \\ -M^{-1}K & -M^{-1}C \end{bmatrix}, \\ B &= \begin{bmatrix} 0_{n\times p} \\ M^{-1}B_s \end{bmatrix}, \\ D &= \begin{bmatrix} 0_{n\times r} \\ M^{-1}D_s \end{bmatrix} \end{aligned} \tag{16}$$

Linear quadratic regulator (LQR) control algorithm is one of the most widely used methods for active control design analysis. By analyzing the geometry model shown in **Figure 1** which is described by (15), the required damping force supplied by the MRF damper is derived by

$$J = \frac{1}{2}\int_{t_0}^{\infty}\left[Z^T(t)QZ(t) + U^T(t)RU(t)\right]dt \tag{17}$$

where Q is positive semidefinite state weighting matrix and R is the positive definite control input weighting matrix. The matrices Q and R determine the relative importance of the error and the expenditure of this energy.

In this study, according to the pipeline vibration control demand, the maximum damping force and the dynamic range of the MRF damper are predetermined as 1400 N and 5, respectively. Based on the MRF damper structure shown in **Figure 3**, the material selection and material properties of the MRF damper are shown in **Table 1.**

The magnetic properties of DT4C, Steel 45, and MRF2035 are shown in **Figures 4**, **5**, and **6**, respectively. The induced yield stress of the MRF2035 as a function of the applied magnetics induction intensity is shown in **Figure 7**.

According to the characteristics of the materials and the specifications of the MRF damper, the parameters of

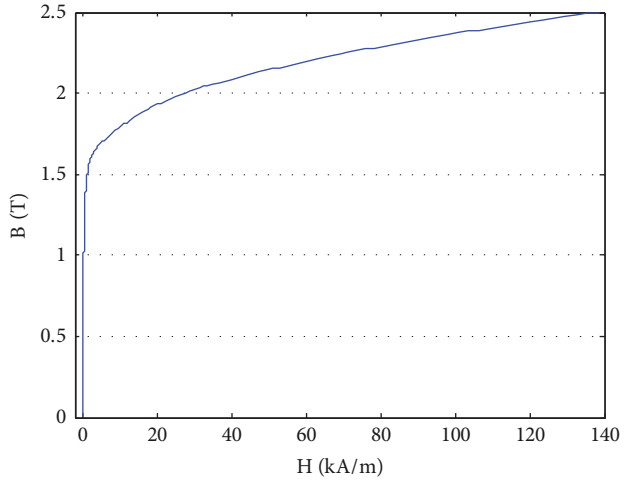

Figure 4: $B - H$ curve of DT4C.

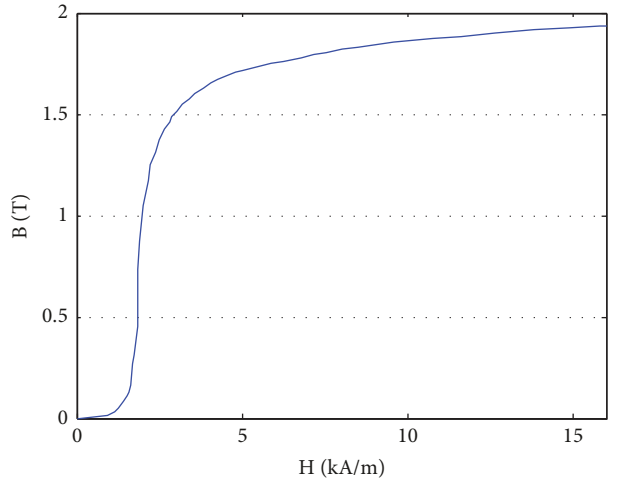

Figure 5: $B - H$ curve of Steel 45.

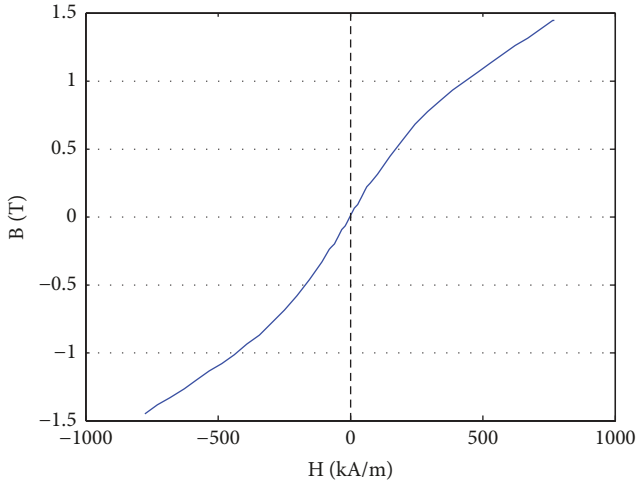

Figure 6: $B - H$ curve of MRF2035.

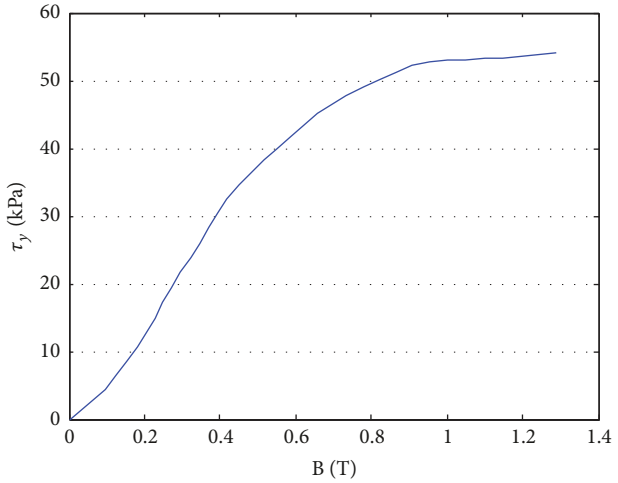

Figure 7: $B - \tau_y$ curve of MRF2035.

the damper could be preliminarily determined as shown in **Table 2**.

2.4. Shear Stress Prediction of MRF Damper. From (13), it can be seen that when the numbers of coil turns and MRF are determined, the magnetic induction intensity of the damper is only determined by the current of the coil. The constitutive equation of magnetic medium for MRF is shown as follows:

$$B_m = \mu_m H_m \tag{18}$$

where H_m is the magnetic field intensity of MRF.

From (13) and (18), the relationship between the current and the magnetic field intensity in the damping gap could be expressed as

$$H_m = \frac{NI}{2h} \tag{19}$$

As the values of N and h in (19) could be found in **Table 2**, the magnetic field intensity in the MRF under different current could be calculated by (19).

The MRF is under the control of the magnetic field generated by the coil in MRF damper. The control current of the MRF damper is given by

$$I(i) = \frac{I_{\max}}{n} \times i \quad (i = 0, 1, 2 \ldots n) \tag{20}$$

According to (20), (19) could be written as

$$H_m(i) = \frac{N}{2h} I(i) \quad (i = 0, 1, 2 \ldots n) \tag{21}$$

Based on the characteristic curve of the MRF shown in **Figure 6**, the interpolating function of $B - H$ relation of the MRF could be described as

$$B_m(i) = P(H_m(i)) \quad (i = 0, 1, 2 \ldots n) \tag{22}$$

With the $B - \tau_y$ data of the MRF, as shown in **Figure 7**, the dynamic yield stress of the MRF in the damping gap could be described as

$$\tau_y(i) = P(B_m(i)) \quad (i = 0, 1, 2 \ldots n) \tag{23}$$

Table 2: Basic structural parameters of MRF damper.

Initial parameters			Design parameters		
Parameters	**Value**	**Unit**	**Parameters**	**Value**	**Unit**
F_f	200	N	F	1414.5	N
h	1	mm	β	6.2	- -
μ_m	$6\pi\times10^{-7}$	H/m	r	12.5	mm
B_m	1	T	L_w	4	mm
B_p	1.5	T	t_y	6	mm
B_y	1.5	T	h_s	6.3	mm
η	0.28	Pa·s	L_c	45	mm
τ_y	52	kPa	$I_{\max}$	4	A
r_p	7.5	mm	d_c	1	mm
$u_{\max}$	0.5	m/s	N	270	turns
J_{tc}	5	A/mm^2	n_c	6	layers

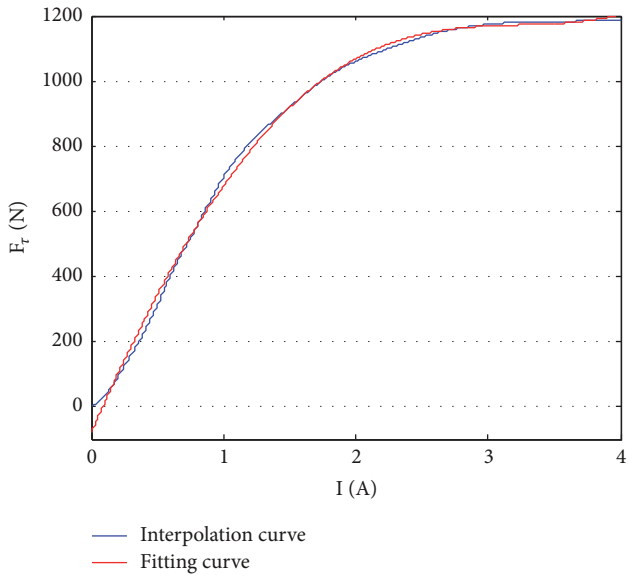

Figure 8: $F_\tau - I$ curve of MRF damper.

From (1), the shear stress of the MRF damper could be calculated as follows:

$$f_\tau(i) = \frac{3LA_P}{h}\tau_y(i) \quad (i = 0, 1, 2 \ldots n) \tag{24}$$

The shear stress of the MRF damper could be obtained by solving (20) ~ (24) in turn, and (22) and (23) are solved by cubic spline interpolation method. The relationship of current and shear stress of the MRF damper is shown in **Figure 8**.

By applying the least-squares curve fitting method, the approximate polynomial curve of the shear stress is shown in **Figure 8** and the corresponding approximate polynomial is

$$F_\tau = 5.376I^4 - 20.616I^3 - 163.161I^2 + 937.390I - 83.217 \tag{25}$$

As shown in **Figure 8**, the shear stress of the proposed MRF damper increases rapidly with the increasing current at lower currents; the growth rate of shear stress gradually slows down at higher currents as the damper starts to saturate. There is a nonlinear relationship between the shear stress and the control current of the MRF damper.

3. Simulation Analysis of MRF Damper

3.1. Fundamentals of the Simulation

3.1.1. Fundamental Equations of Electromagnetic Field. The electromagnetic analysis on the macro level is to solve the Maxwell equation group under certain boundary conditions. Maxwell's equations could be written in differential or integral form, stating the relationships between the fundamental electromagnetic quantities [35]. The differential form is presented here because it leads to differential equations that the finite element method (FEM) could handle. For general time-varying fields, Maxwell's equations could be written as

$$\begin{aligned} \nabla \times H &= J + \frac{\partial D}{\partial t} \\ \nabla \times E &= -\frac{\partial B}{\partial t} \\ \nabla \bullet D &= \rho \\ \nabla \bullet B &= 0 \end{aligned} \tag{26}$$

where H is the magnetic field intensity, J is the electric current density, D is the electric flux density, E is the electric field intensity, B is the magnetic flux density, and ρ is the electric charge density.

Another fundamental equation is the continuity equation:

$$\nabla \bullet J = -\frac{\partial \rho}{\partial t} \tag{27}$$

To obtain a closed system, the equations include constitutive relations that describe the macroscopic properties of the medium [36]. They are given as

$$D = \varepsilon E$$
$$B = \mu H \quad (28)$$
$$J = \sigma E$$

where ε is the permittivity of material, μ is the permeability of material, and σ is the electrical conductivity of material. By combining the above equations, a closed system of equations could be formed, which could analyze and calculate the electromagnetic field. It constitutes the theoretical basis for the FEM to calculate the electromagnetic field.

3.1.2. Boundary and Physics Interface Conditions. To get a full description of an electromagnetics problem, boundary conditions must be specified at material interfaces and physical boundaries [37]. At interfaces between two media, the boundary conditions could be expressed mathematically as

$$n_{ij} \times \left(E_i - E_j\right) = 0$$
$$n_{ij} \times \left(D_i - D_j\right) = \rho_s$$
$$n_{ij} \times \left(H_i - H_j\right) = J_s \quad (29)$$
$$n_{ij} \times \left(B_i - B_j\right) = 0$$

where n_{ij} is the outward normal from medium two, ρ_s is the surface charge density, and J_s is the surface current density.

From these relationships, the interface condition is derived for the current density.

$$n_{ij} \bullet \left(J_i - J_j\right) = -\frac{\partial \rho_s}{\partial t} \quad (30)$$

3.1.3. Electromagnetic Heat Source. Due to the Joule heat effect, the energized electromagnetic coil would produce Joule heat. Joule heat was transmitted in the MRF damper and eventually radiated into the air through the piston rod, the cylinder, and the end covers of the damper. When the Joule heat of the MRF damper is equal to the heat dissipation, the temperature of the damper will remain unchanged. The coil temperature rise will change the physical properties of the MRF and the damping force and the dynamic range of the damper will also be affected. Although the influence of temperature on the damping force of MRF damper is not significant [38], high temperature and the long time for MRF damper are very detrimental. The Joule heat could be expressed as

$$Q_e = J \bullet E \quad (31)$$

where Q_e is the electromagnetic heat source.

When the piston of the MRF damper is stationary, the resistive heating in the heat equation is

$$Q_e = \rho C_p \frac{\partial T}{\partial t} - \nabla \bullet (k \nabla T) \quad (32)$$

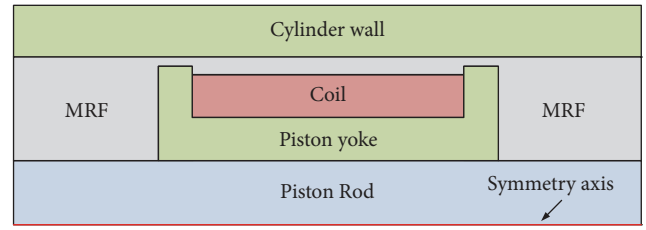

Figure 9: 2D axisymmetric geometric model of MRF damper.

where ρ is the density, C_p is the heat capacity, T is the temperature, and k is the thermal conductivity.

3.2. MRF Damper Finite Element Modeling and Simulation

3.2.1. Magnetic Field Analysis of the MRF Damper. For computational time reduction, the computational domain is reduced to a 2D axisymmetric model. Based on the structure of the magnetic circuit shown in **Figure 3** and the structural parameters in **Table 2**, a 2D axisymmetric geometric model of the MRF damper is established in COMSOL as shown in **Figure 9**.

According to the magnetic properties of the materials shown in **Figures 4**, **5**, and **6**, the magnetic property of the materials is configured in the material interface of COMSOL software. The graph of the flux density distribution of the damper at different currents is shown in **Figure 10**.

As shown in **Figure 10**, when the electromagnetic coil is energized, a closed magnetic circuit is formed in the MRF damper, and then the magnetic induction lines are evenly distributed. The magnetic flux density in the damper increases with the rising current. The distribution of magnetic induction lines and magnetic flux density in the damper are in accordance with the design expectations.

3.2.2. Magnetic Field Analysis of the MRF Damper with Magnetism-Insulators. As can be seen from **Figure 10**, it is easy to find that some of the magnetic induction lines enter the cylinder wall through other parts of the damper rather than the damping gap, which causes the magnetic induction intensity at the damping gap to be lower than the theoretical value. In order to avoid this phenomenon, a 2D axisymmetric geometric model of MRF damper with magnetism-insulators is established as shown in **Figure 11**.

The magnetic field of the MRF damper with magnetism-insulators is shown in **Figure 10**.

By comparing **Figure 10** with **Figure 12**, it could be found that the method of installing magnetism-insulators on both ends of the piston yoke could improve the distribution of the magnetic induction lines in the MRF damper. However, the improvement effect is not significant. The average magnetic induction intensity of the two structures in the damping gap is shown in **Figure 13**.

As shown in **Figure 13**, when the current is 4 A, the magnetic induction intensity of the damper with magnetism-insulators is just 0.04 T higher, which means that the utilization of the magnetic field could not be effectively increased

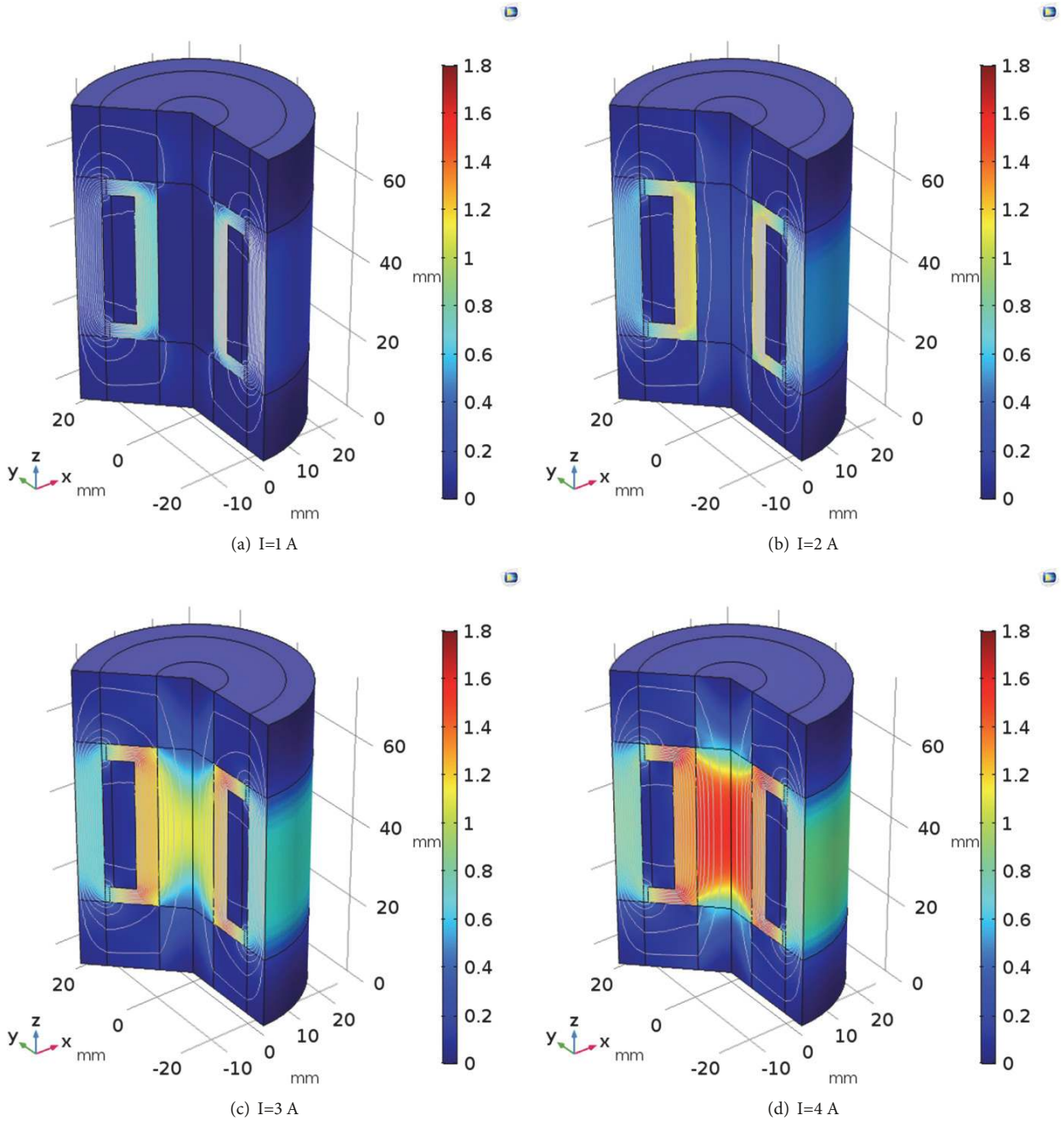

(a) I=1 A (b) I=2 A

(c) I=3 A (d) I=4 A

Figure 10: Magnetic field of the MRF damper.

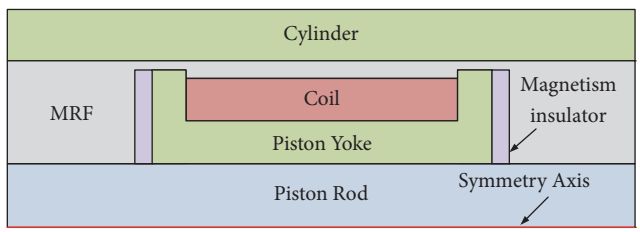

Figure 11: 2D axisymmetric geometric model of MRF damper with magnetism-insulators.

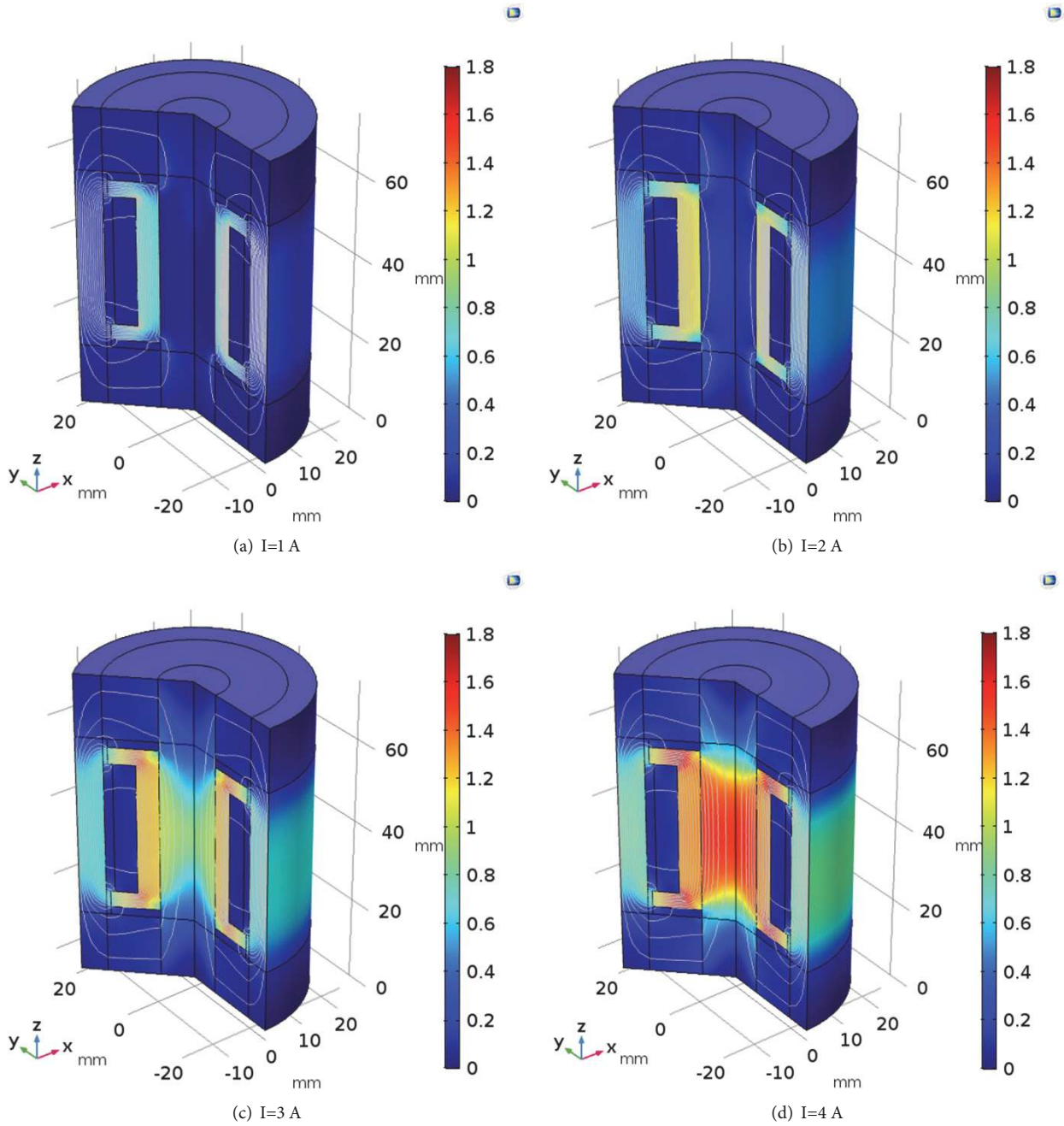

(a) I=1 A (b) I=2 A

(c) I=3 A (d) I=4 A

Figure 12: Magnetic field of the MRF damper with magnetism-insulators.

by installing magnetism-insulators on both ends of the piston yoke.

3.3. Damping Force Analysis. From (1), it can be seen that the viscous stress and shear stress of the MRF damper are enhanced with the increase of the flange width. As the magnetism-insulators change the width of the flange and the distribution of the magnetic field, the performance of the damper will also be changed. Because of the different magnetic permeability of the magnetism-insulators and the flange, the distribution of magnetic field in the damping gap is not uniform. Therefore, (1) is not suitable for calculating the shear stress of the MRF damper with magnetism-insulators. In addition, when (1) is used to calculate the shear stress of the MRF damper, the magnetic properties of the material and the magnetic flux leakage could not be fully considered. However, by using the software based on the FEM, almost all the factors that affect the damping force of the MRF damper could be considered, which could avoid the neglect and approximation problems in numerical calculation.

Table 3: Working temperature of the components.

Component	MRF2035	Stepseal	Enameled wire	Pouring sealant
Maximum temperature	130°C	200°C	150°C	180°C

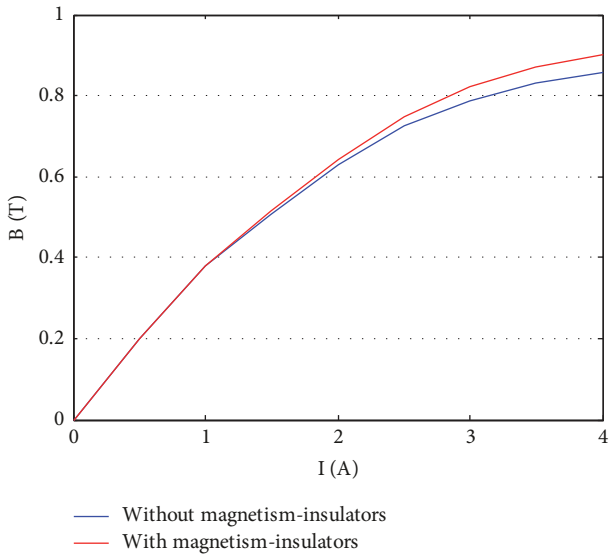

Figure 13: Average magnetic induction intensity in the damping gap.

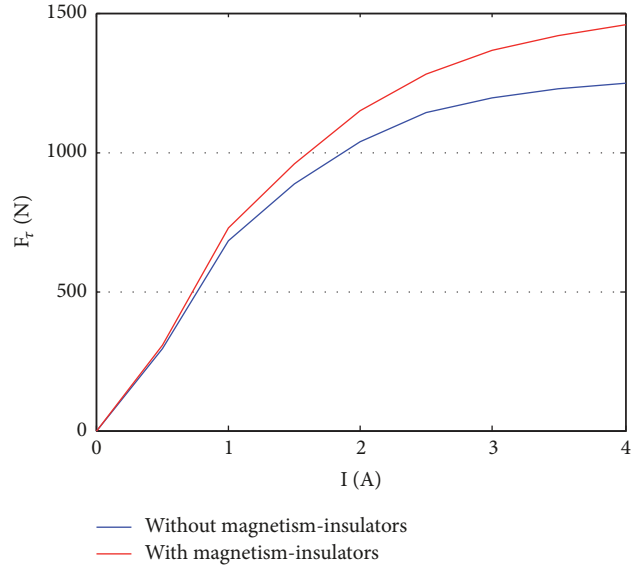

Figure 14: Shear stress at different currents.

From **Figure 7**, the relationship between shear yield strength and magnetic flux density of MRF2035 could be expressed as

$$\tau_y = f_\tau(B_l) \tag{33}$$

where B_l is the magnetic induction intensity in the damping gap.

From (1) and (29), the integral form of the shear stress of the damper could be expressed as

$$F_\tau = \int_0^L \frac{3 \times f_\tau(B_l) \times A_P}{h} dl \tag{34}$$

By using the linear integral function of COMSOL, (30) could be established and solved. The relationship of current and shear stress of the two dampers is shown in **Figure 14**.

As shown in **Figure 14**, when the current is 4 A, the shear stress of the two dampers is 1251.4 N and 1454.6 N, respectively. Through the above analysis, the MRF damper with magnetism-insulators has the advantages of lowering magnetic leakage and increasing shear stress of the damper. However, it also has the disadvantages of increasing the vicious stress, the length of piston yoke, and the difficulty of design and analysis of MRF dampers. Therefore, it is not advisable to add magnetism-insulators at both ends of the piston yoke.

3.4. Electromagnetic-Thermal Coupling Simulation of the MRF Damper. The performance of MRF dampers is influenced by many factors; temperature is one of the main factors [39]. Few scholars had considered the problem of electromagnetic heating of the coil, when designing MRF dampers. The MRF damper proposed in this paper has the characteristics of compact structure, small volume, and high power density. Therefore, it is necessary to study the electromagnetic heat effect of the damper to ensure that the design method proposed in this paper could meet the practical application requirements. The electromagnetic-thermal coupling simulation of the damper is carried out by using the heat transfer module and the electromagnetic heat source coupling interface of COMSOL. During the simulation the ambient temperature is 20°C; the convection heat transfer coefficient of air is 5 W/(m^2·K) [40].

According to the above conditions and parameters in **Table 2**, the multiphysics simulation model of the damper is configured, and the temperature field of the damper with different currents is simulated. The heat distribution in the MRF damper under different currents is shown in **Figures 15** and **16**. The maximum temperature under different control currents is shown in **Figure 17**.

As can be seen from **Figures 15** and **16**, the transient temperature field of the two MRF dampers presents an uneven gradient distribution and the highest temperature appears at the coil. By observing the current-temperature curves shown in **Figure 17**, it could be found that the temperatures of the two MRF dampers increase with the rising current and the temperature curves of the two MRF dampers almost overlap. When the current is 4 A, the maximum temperatures of the two MRF dampers are 70.71°C and 70.67°C, respectively. The maximum operating temperature of the main components is shown in **Table 3**.

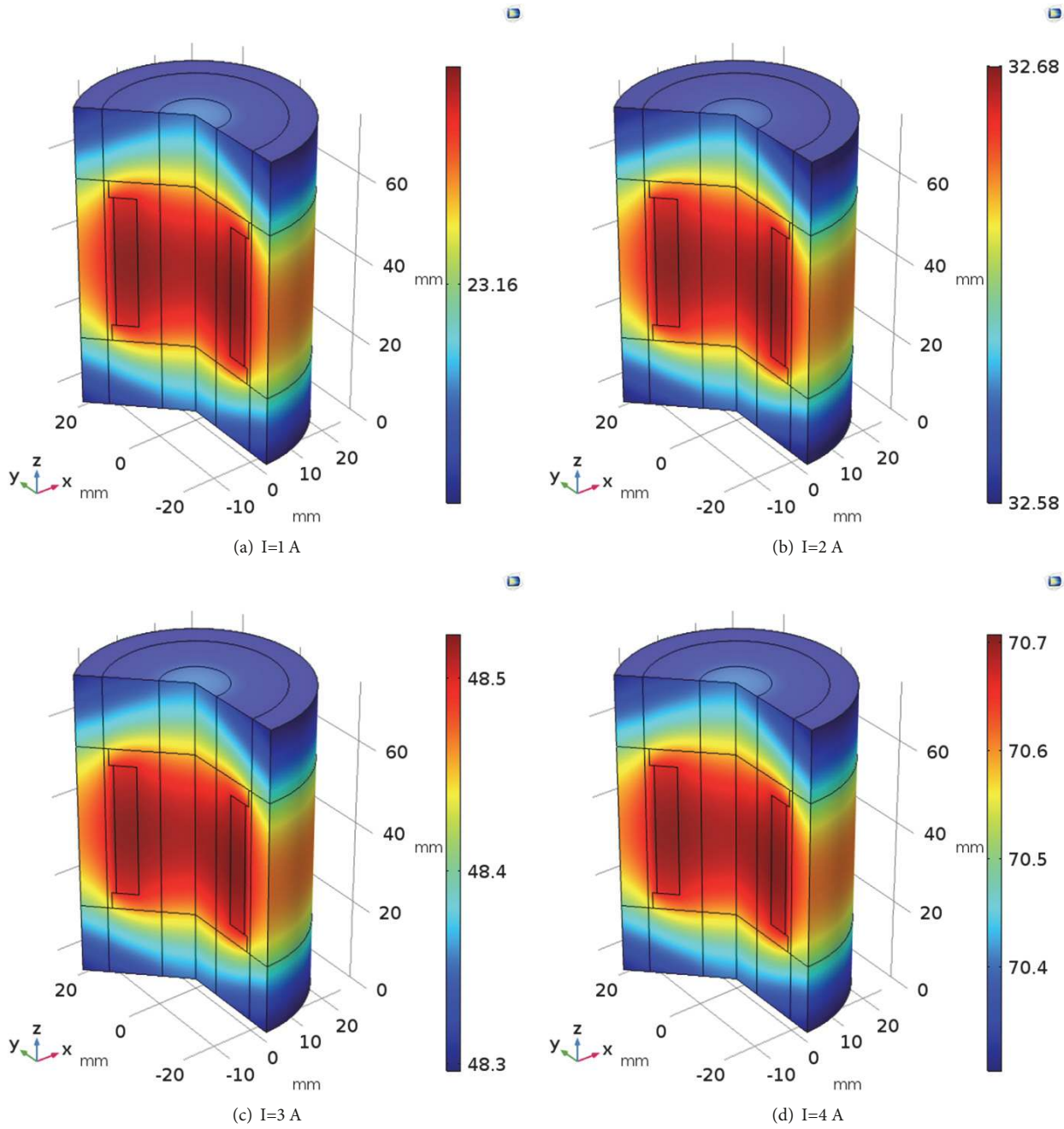

Figure 15: Heat distribution in the MRF damper.

It can be seen from **Table 3** that the maximum working temperature of the damper is 130°C, which is much higher than temperature generated by the coil. Meanwhile, the current of the coil is determined by the control strategy and the characteristics of the vibration source, and the maximum current will not be maintained for a long time. The simulation results show that the coil could meet the heat dissipation requirements of the proposed MRF damper.

4. Experimental Setup

According to the structural parameters of the proposed MRF damper, two double-ended shear-valve mode MRF damper prototypes are fabricated in accordance with the characteristics of pipeline vibration. The testing system is shown in **Figure 18**. This testing system includes three main components: INSTRON-8801 test system, MRF damper prototype, and current controller.

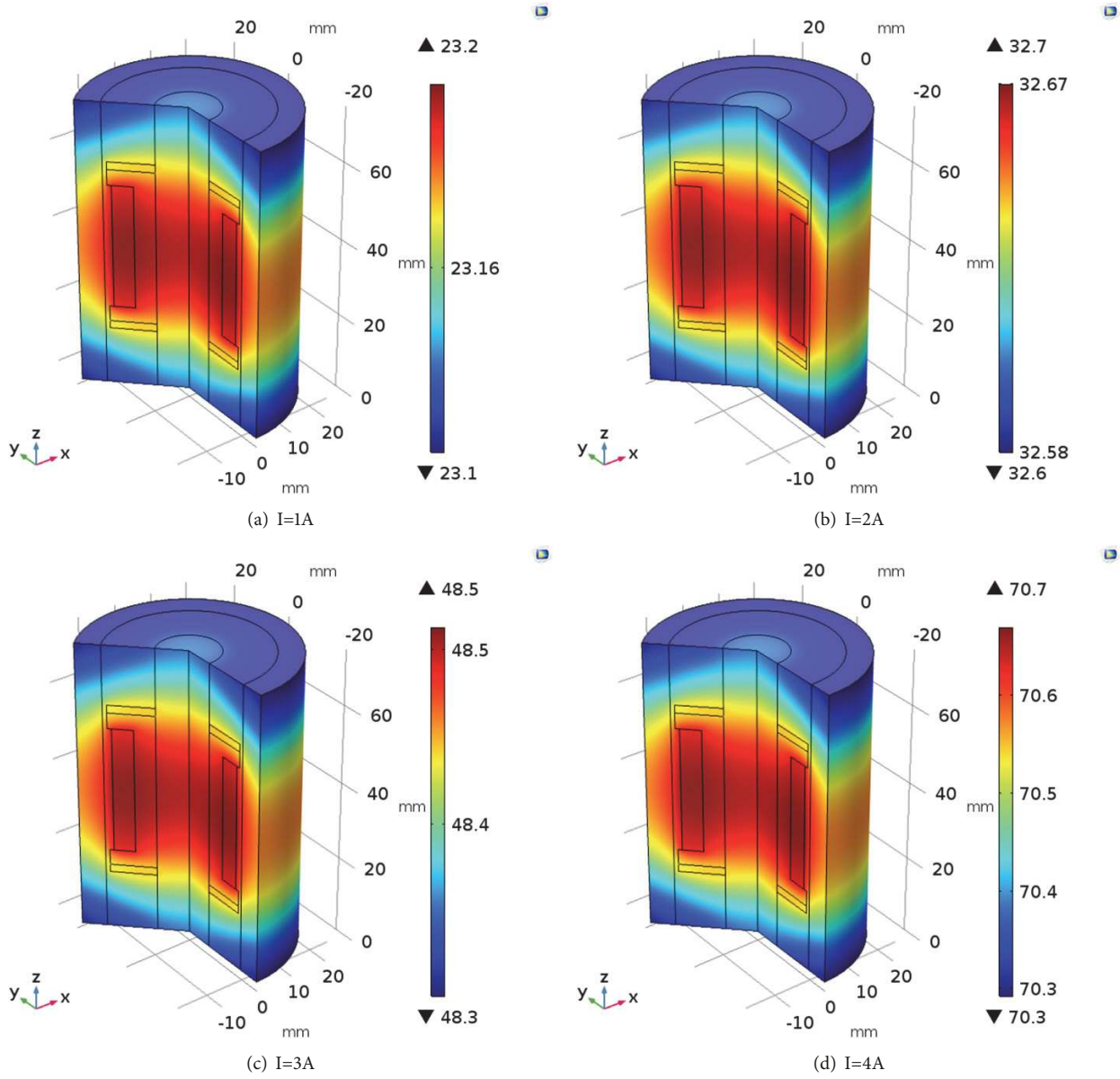

(a) I=1A (b) I=2A

(c) I=3A (d) I=4A

Figure 16: Heat distribution in the MRF damper with magnetism-insulators.

Sinusoidal wave is used as the excitation to get the displacement and velocity of the damper piston. The test machine was set at a sinusoidal loading with a displacement amplitude of 5 mm and frequency of 1 Hz, 2 Hz, 5 Hz, and 10 Hz, respectively. Meanwhile, The applied control currents range from 0 A to 4 A.

5. Results and Discussions

The damping force of the MRF damper under the different loading frequencies, different displacement amplitudes, and different currents are shown as follows.

From **Figures 19–22**, it could be seen that the damping force of the proposed MRF damper is enhanced with the increasing current, initially at a faster rate and eventually at a slower rate. As the current increases from 0 A to 1.5 A, the damping force is significantly proportional to the increment of the current. When the current exceeds 1.5 A, as the current increases, the damping force slightly increases. When the current is 0 A, the uncontrollable damping force equals about 324 N, which is due to the viscous effect of the MRF and the friction force. In addition, when the applied current is 4 A, the maximum damping force is 1587 N, which denotes that the controllable force due to MR effect is about 1263 N and the dynamic range is 4.63. It is obvious that as the displacement and the velocity change, the damping force is slightly influenced under the same current, which implies that the damping force of the MRF damper is not critically dependent on the frequency and the velocity.

Figure 23 shows the calculated, simulated, and measured shear stress of the proposed MRF damper under different control currents. With increment of the current, calculated,

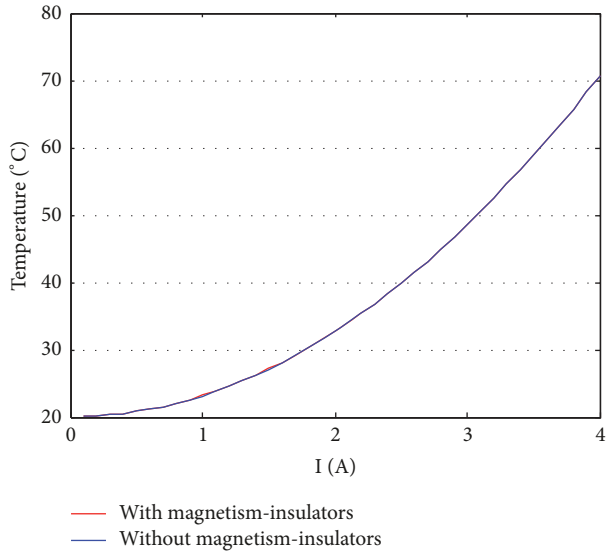

Figure 17: Maximum temperature at different currents.

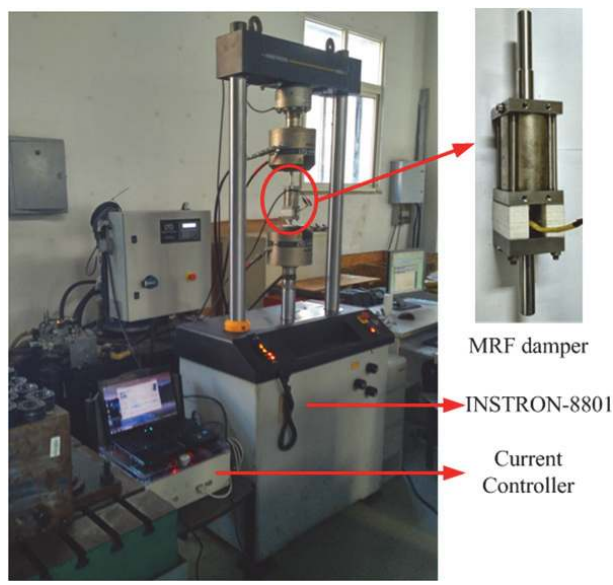

Figure 18: Damping force testing platform.

simulated, and measured shear stress increase. It is clearly observed that the calculated and simulated shear stress are in comparative agreement with the measured shear stress, verifying the effectiveness of the constructed damping force model.

However, as shown in **Figure 23**, the experimental results are slightly larger than the simulation and the theoretical ones. The maximum deviation between the experimental value and the theoretical value is 75.1 N and 12.8 N between the experimental value and simulation value. It also could be found that when the current is greater than 3A, the theoretical value of shear stress tends to be constant, but the experimental value continues to increase with the increasing current. From **Figure 3**, it can be seen that an annular gap is formed by the coil and the cylinder wall, which is similar to the damping gap that formed by the yoke flange and the cylinder wall. As the current increases, the saturation in the magnetic circuit of the MRF damper is more significant and the magnetic field intensity in the annular gap increases, which leads to the enhancement of the shear stress. However, the damping force generated by the annular gap is neglected in the theoretical calculations, which caused the difference between theoretical value and measured value. Since the shear stress caused by the annular gap is taken into account in the simulation model, the simulation value of the damping force is closer to the actual value.

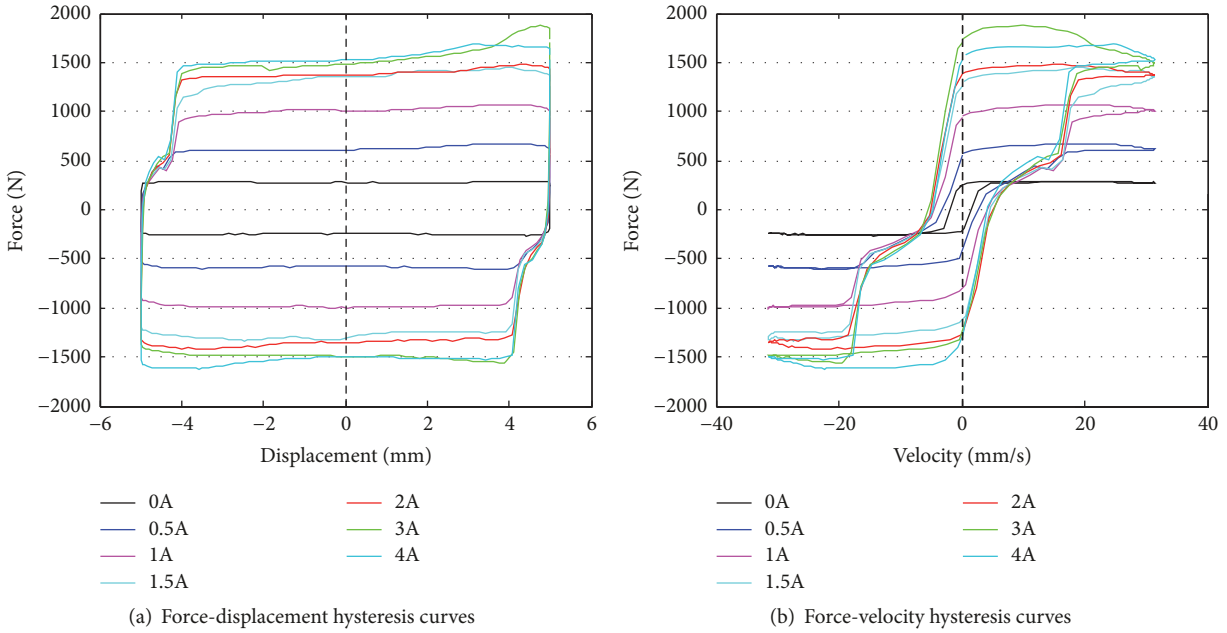

(a) Force-displacement hysteresis curves (b) Force-velocity hysteresis curves

Figure 19: Hysteresis curves under different drive current at frequency of 1 Hz.

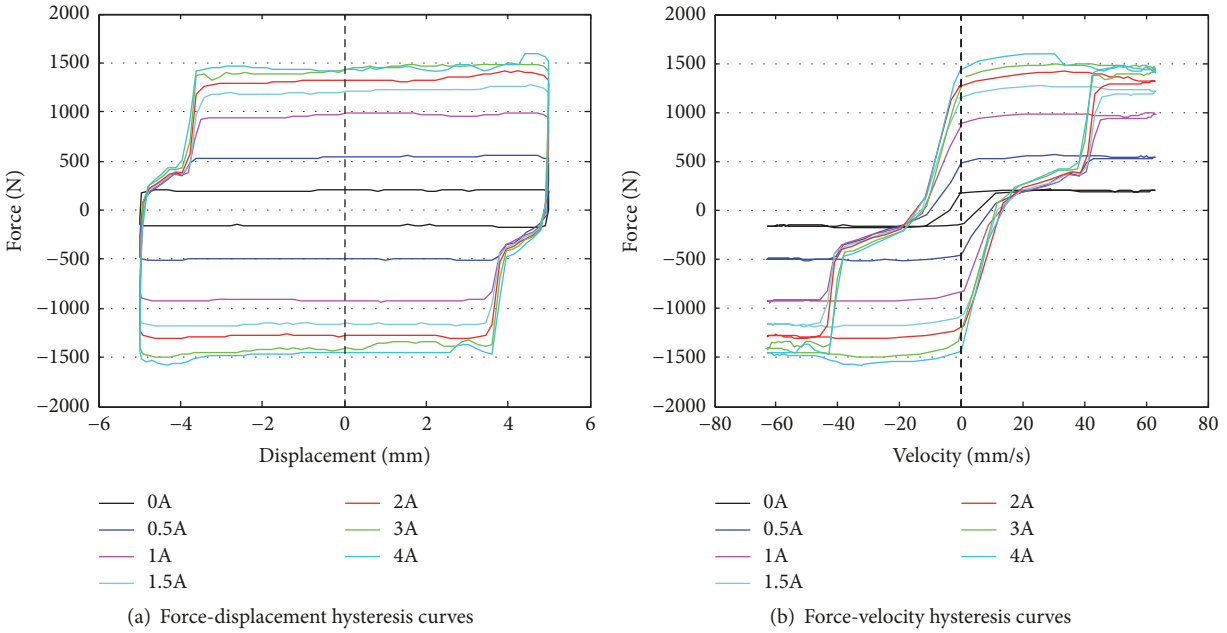

(a) Force-displacement hysteresis curves (b) Force-velocity hysteresis curves

Figure 20: Hysteresis curves under different drive current at frequency of 2 Hz.

6. Conclusions

In this paper, a double-ended and shear-valve mode MRF damper for pipeline vibration control application is designed, simulated, fabricated, and experimentally tested. The design concept for the proposed MRF damper was described in detail. Based on the proposed analytical method, calculations were performed concerning the principal characteristics of the MRF damper. The mathematical model of the proposed MRF damper was derived to predict damping performance, which could directly relate the shear stress to the control current. The principle of the proposed MRF damper is validated and the simulation of magnetic field and electromagnetic-thermal field is performed by FEA using COMSOL software. To reduce the magnetic leakage and improve the magnetic induction intensity in the damping gap, MRF damper with magnetism-insulators is proposed, simulated, and compared with the dampers without magnetism-insulators. In order to prove the analytical results, experimental tests are performed as well. The experimental maximum damping force and

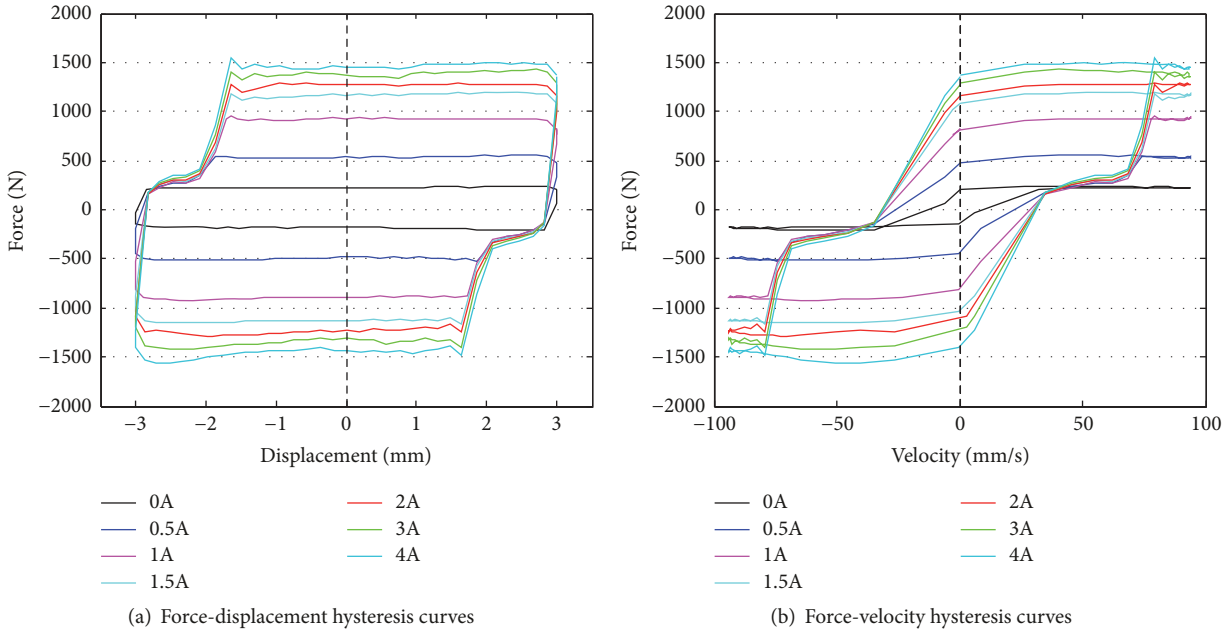

(a) Force-displacement hysteresis curves (b) Force-velocity hysteresis curves

Figure 21: Hysteresis curves under different drive current at frequency of 5 Hz.

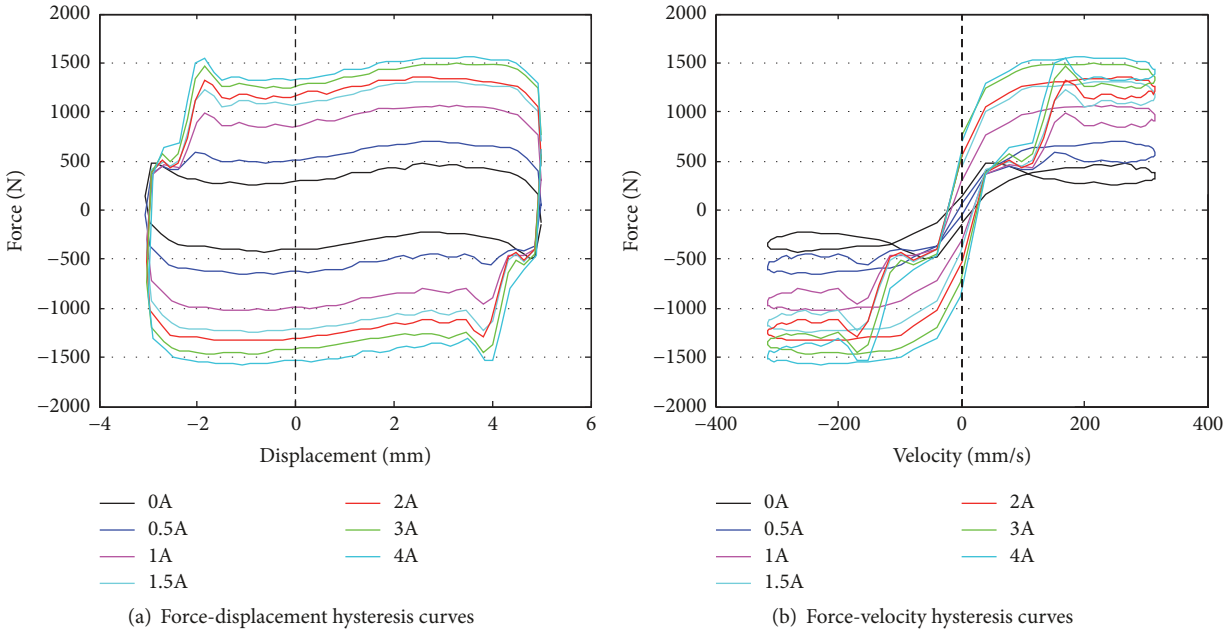

(a) Force-displacement hysteresis curves (b) Force-velocity hysteresis curves

Figure 22: Hysteresis curves under different drive current at frequency of 10 Hz.

the dynamic range are 1587 N and 4.63, respectively, which are very close with the designed maximum damping force (1400 N) and the dynamic range (5) obtained in MRF damper design process. The experimental results validate the reasonableness and effectiveness of the theoretical analysis and the simulation model. The test results also indicate that the damping force of the MRF damper increases obviously with the rise of the control currents until magnetic saturation occurred, and the effect of displacement and velocity on the damping force is far smaller than the current.

Data Availability

The datasets generated and/or analyzed during the current study are available from the corresponding author on reasonable request.

Conflicts of Interest

The authors declare that there are no conflicts of interest regarding the publication of this article.

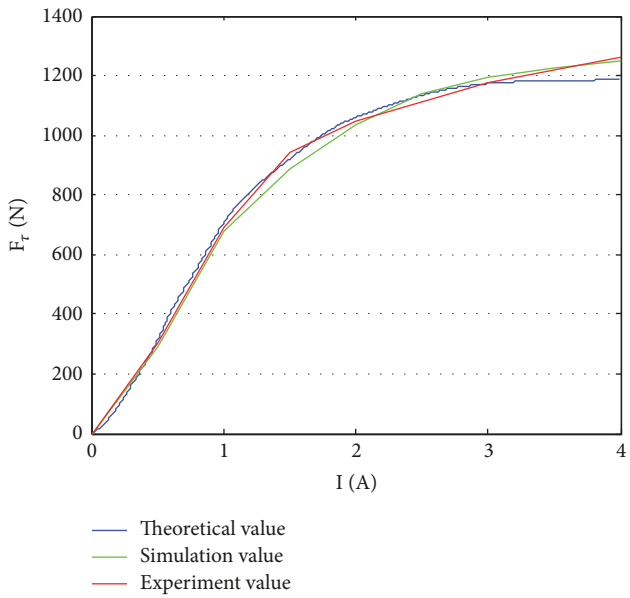

Figure 23: Shear stress of the MRF damper.

Acknowledgments

This work was funded by the Equipment Pre-Research Project of 2017 (no. 61402100104), National Natural Science Foundation of China (nos. 51705008 and 11572012), Beijing Natural Science Foundation (nos. 3182003 and 1184012), China Postdoctoral Science Foundation Funded Project (no. 2017M620551), and Beijing Postdoctoral Research Foundation (no. 2017-ZZ020).

References

[1] A. Raizada, P. Singru, V. Krishnakumar, and V. Raj, "Development of an Experimental Model for a Magnetorheological Damper Using Artificial Neural Networks (Levenberg-Marquardt Algorithm)," *Advances in Acoustics and Vibration*, pp. 1–6, 2016.

[2] D. Yu, J. Wen, H. Zhao, Y. Liu, and X. Wen, "Vibration reduction by using the idea of phononic crystals in a pipe-conveying fluid," *Journal of Sound and Vibration*, vol. 318, no. 1-2, pp. 193–205, 2008.

[3] S. Chen and Y. Ma, "Seismic responses of isolated continuous girder bridges based on hybrid control of MRD and LRB," *Journal of Beijing University of Technology*, vol. 39, no. 3, pp. 378–384, 2013.

[4] K. Rama Raju and D. Vineeth Varma, "Developments in vibration control of structures and structural components with magnetorheological fluids," *Current Science*, vol. 112, no. 3, pp. 499–508, 2017.

[5] X. Bai and W. Norman, "A fail-safe magnetorheological energy absorber for shock and vibration isolation," *Journal of Applied Physics*, vol. 115, no. 17, p. 17B535, 2014.

[6] R. Zemp, J. Carlos, and H. Saldias, "Development of a long-stroke MR damper for a building with tuned masses," *Smart Materials and Structures*, vol. 25, no. 10, pp. 101–106, 2016.

[7] G. Heo, C. Kim, and C. Lee, "Experimental test of asymmetrical cable-stayed bridges using MR-damper for vibration control," *Soil Dynamics and Earthquake Engineering*, vol. 57, pp. 78–85, 2014.

[8] M. Rahman, Z. C. Ong, and S. Julai, "A review of advances in magnetorheological dampers: their design optimization and applications," *Journal of Zhejiang University-Science A*, vol. 18, no. 12, pp. 991–1010, 2017.

[9] D. R. Mcintyre and E. Ford, "Recent developments in the analysis of fires, explosions, and production disruption incidents in chemical plants and oil refineries," *Process Safety Progress*, vol. 28, no. 3, pp. 250–258, 2009.

[10] P. Ranjan, R. Balasubramaniam, and V. K. Jain, "Analysis of magnetorheological fluid behavior in chemo-mechanical magnetorheological finishing (CMMRF) process," *Precision Engineering*, vol. 49, pp. 122–135, 2017.

[11] H. Nishiyama, S. Fushimi, and M. Nakano, "Numerical simulation of MR fluid damping characteristics using a modified Bingham model," *Journal of Intelligent Material Systems and Structures*, vol. 13, no. 10, pp. 647–653, 2002.

[12] S. Cetin, E. Zergeroglu, S. Sivrioglu, and I. Yuksek, "A new semiactive nonlinear adaptive controller for structures using MR damper: design and experimental validation," *Nonlinear Dynamics*, vol. 66, no. 4, pp. 731–743, 2011.

[13] Y.-J. Nam and M.-K. Park, "Electromagnetic design of a magnetorheological damper," *Journal of Intelligent Material Systems and Structures*, vol. 20, no. 2, pp. 181–191, 2009.

[14] F. A. Shirazi, J. Mohammadpour, K. M. Grigoriadis, and G. Song, "Identification and control of an MR damper with stiction effect and its application in structural vibration mitigation," *IEEE Transactions on Control Systems Technology*, vol. 20, no. 5, pp. 1285–1301, 2012.

[15] H.-W. Chen and Q. Zhang, "Design of horizontal axis washing machine with ball balancer and MR dampers," *International Journal of Precision Engineering and Manufacturing*, vol. 18, no. 12, pp. 1783–1793, 2017.

[16] W. H. Kim, J. H. Park, and S. Kaluvan, "A novel type of tunable magnetorheological dampers operated by permanent magnets," *Sensors and Actuators A: Physical*, pp. 104–117, 2017.

[17] Y.-J. Nam and M.-K. Park, "Performance evaluation of two different bypass-type MR shock dampers," *Journal of Intelligent Material Systems and Structures*, vol. 18, no. 7, pp. 707–717, 2007.

[18] Z. Parlak, T. Engin, and I. Çalli, "Optimal design of MR damper via finite element analyses of fluid dynamic and magnetic field," *Mechatronics*, vol. 22, no. 6, pp. 890–903, 2012.

[19] T. M. Gurubasavaraju, H. Kumar, and A. Mahalingam, "An approach for characterizing twin-tube shear-mode magnetorheological damper through coupled FE and CFD analysis," *Journal of the Brazilian Society of Mechanical Sciences and Engineering*, vol. 40, no. 3, pp. 185-121, 2018.

[20] R. Ahamed, M. M. Rashid, and M. M. Ferdaus, "Design and modeling of energy generated magneto rheological damper," *Korea-Australia Rheology Journal*, vol. 28, no. 1, pp. 67–74, 2016.

[21] P. Mitrouchev, A. Klevinskis, and V. Bucinskas, "Analytical research of damping efficiency and heat generation of magnetorheological damper," *Smart Materials and Structures*, pp. 1–11, 2017.

[22] M. S. A. Khan, A. Suresh, and N. S. Ramaiah, "Numerical study of magnetic circuit response in magneto-rheological damper," *Journal of Engineering, Design and Technology*, vol. 14, no. 1, pp. 196–210, 2016.

[23] Y. Zhao, "Study on load modeling and driving application for magneto-rheological fluid damper," *Chongqing University*, pp. 55–78, 2013.

[24] W. Yan, J. Ji, H. Ge et al., "Magnetic circuit design and experimental study on the inverse MR dampers," *Journal of Beijing University of Technology*, vol. 7, pp. 592–595, 2006.

[25] R. Ahamed, M. M. Rashid, M. M. Ferdaus, and H. M. Yusof, "Design and modeling of energy generated magneto rheological damper," *Korea-Australia Rheology Journal*, vol. 28, no. 1, pp. 67–74, 2016.

[26] X. Guan, J. Li, and J. Ouyang, "Magnetic and mechanical performance of magnetorheological fluid damper with different dimension," *Journal of Functional Materials*, vol. 7, pp. 1169–1172, 2006.

[27] Z. Hou, *Study of the Properties of MR Damper and Optimal Desigh*, Ningbo University, 2010.

[28] J. Li, D. Wang, J. Duan, H. He, Y. Xia, and W. Zhu, "Structural design and control of a small-MRF damper under 50 N soft-landing applications," *IEEE Transactions on Industrial Informatics*, vol. 11, no. 3, pp. 612–619, 2015.

[29] Z. Liu, "The design and the research of magnetorheological dampers," *Wuhan University of Technology*, pp. 12–36, 2002.

[30] L. Huang, J. Li, and W. Zhu, "Mathematical model of a novel small magnetorheological damper by using outer magnetic field," *AIP Advances*, vol. 7, no. 3, pp. 1–12, 2017.

[31] M. M. Ferdaus, M. M. Rashid, M. H. Hasan, and M. A. Rahman, "Optimal design of Magneto-Rheological damper comparing different configurations by finite element analysis," *Journal of Mechanical Science and Technology*, vol. 28, no. 9, pp. 3667–3677, 2014.

[32] X. Guan, P. Guo, and J. Ouyang, "Multi-objective optimization of magnetorheological fluid dampers," *Pacific Science Review*, vol. 10, no. 3, pp. 351–357, 2008.

[33] G. Hu, F. Liu, Z. Xie, and M. Xu, "Design, analysis, and experimental evaluation of a double coil magnetorheological fluid damper," *Shock and Vibration*, pp. 1–12, 2016.

[34] C. Lin, "Design and research of electromagnetic low-frequency vibration energy harvesting devices," *Zhejiang University of Technology*, vol. 3, no. 10, pp. 26-27, 2013.

[35] J. P. A. Bastos and N. Sadowski, *Magnetic Materials and 3D Finite Element Modeling*, CRC Press, 2014.

[36] Z. Yu, S. Liu, N. Zhang, and W. Li, "Multi-field coupling simulation analysis of MR damper," *Journal of Agricultural Machinery*, vol. 45, no. 1, pp. 1–7, 2014.

[37] COMSOL, COMSOL Multiphysics Reference Manual [M]. Version: COMSOL 5.3, pp. 799-832, 2017.

[38] D. G. Breese, F. Gordaninejad, and S. Liu, "Heating of magneto-rheological fluid dampers: a theoretical study," *Smart Structures and Materials: Smart Systems for Bridges, Structrues, and Highways*, vol. 2, p. 348, 1999.

[39] G. Geldhof, *Semi-active Vibration Dynamics Control of Multi-Cart Systems Using a Magnetorheological Damper*, University of Technology, 2013.

[40] X. Dong, J. Yu, and M. Yang, "Optimization and experimental study of magneto-rheological fluid damper considering temperature effects," *Journal of Vibration and Shock*, vol. 35, no. 8, pp. 54–59, 2016.